Astronomy & Astrophysics manuscript no. main
July 24, 2026
©ESO 2026

Atmosphere mitigation in CMB observations using multi-frequency time-domain component separation

Julien Tang[1,2,3]⋆, Shamik Ghosh[3], Jacques Delabrouille[1,3], John C. Groh[3], Oliver Jeong[1,3], Reijo Keskitalo[3,4], and Theodore Kisner[3,4]

[1] CNRS-UCB International Research Laboratory, Centre Pierre Binétruy, IRL2007, CPB-IN2P3, Berkeley, CA 94720, USA
[2] Astroparticule et Cosmologie, Université Paris Cité, CNRS, F-75013 Paris, France
[3] Lawrence Berkeley National Laboratory, 1 Cyclotron Road, Berkeley, CA 94720, USA
[4] Space Sciences Laboratory at University of California, 7 Gauss Way, Berkeley, CA 94720

Received July 30, 2026

ABSTRACT

CMB observations from ground-based observatories are limited in sensitivity by the fluctuating emission from the Earth's atmosphere, mostly due to water vapor inhomogeneities. Even in atmospheric windows, this spurious signal remains the major source of contamination of the data. Traditional mitigation techniques include low-frequency filtering, or for polarization measurements specifically, modulation with a rotating half-wave plate. The first method filters out a significant fraction of the target cosmological signal while the second leaves residuals due to imperfections, temperature to polarization leakage, or polarized atmospheric emission. In this work, we present a new data analysis framework, based on estimation of atmosphere emission templates using a multi-frequency focal plane. The core novelty of this setup is to have detectors dedicated to atmosphere monitoring, allowing for removing atmospheric contamination with time-domain component separation techniques. We introduce a multipole-dependent atmospheric decontamination factor $A_\ell^{\rm atm}$ to quantify the relative reduction of the atmospheric contamination angular power spectrum achievable with this approach. We demonstrate that this decontamination factor scales as the inverse of the survey time and that, using that criterion, our component separation pipeline can outperform a classical filter-bin map-making pipeline by a factor of 4000 for $30 \leq \ell \leq 300$.

arXiv:2607.21432v1 [astro-ph.IM] 23 Jul 2026

1. Introduction

The Cosmic Microwave Background (CMB), relic radiation emitted when light nuclei and electrons in the primordial plasma first combined to form the first neutral atoms, is key to understanding some of the most fundamental questions about our universe, its time evolution and matter-energy content, and about the laws of physics that govern the physics of particles and fields.

CMB observations from ground-based observatories are strongly contaminated by fluctuating emission from the Earth's atmosphere. Fluctuations of the water-vapor content along the line of sight, in particular, generate signals in the data streams that outshine the target CMB signal by several orders of magnitude at all scales. This atmospheric emission is highly non-stationary and depends on time-varying quantities such as the wind speed, the distribution of water vapor inhomogeneities, and the time-varying presence of clouds in the atmosphere, which makes it difficult to describe with a simple statistical model. To avoid excessive contamination of CMB observations by atmospheric emission, data acquired at times when the precipitable water vapor (PWV) exceeds an acceptable level are discarded. The observing efficiency, and hence the mapping speed, is reduced by a factor ranging from 0.63 to 0.86, as a function of observing frequency and telescope type, for CMB observations from the Atacama plateau (Simon et al. 2026). For data passing this weather cut, the residual contamination, averaged down by accumulating years of repeated observations of the same patch of sky, still strongly reduces the sensitivity of the final observed CMB maps. This is true, in particular, on large angular scales where residual atmosphere contamination can be orders of magnitude larger than the ideal instrumental white noise level for large aperture telescopes (LATs) with no polarization modulation, as is the case for ACT (Naess et al. 2025).

For polarization measurements using Small-Aperture Telescopes (SATs) such as those of the Simons Observatory (Ade et al. 2019), the contamination by unpolarized atmospheric signals can be strongly reduced by modulation using a rotating Half-Wave Plate (HWP). However, for LATs, the size of the optics does not allow for the deployment of a HWP as a first optical element. For dual-polarization focal-plane pixels, pair differencing also reduces timeline contamination by unpolarized atmosphere signals, even if the cancellation is not always perfect. In all cases, but particularly so for intensity mappingthe minimization of atmospheric contamination also involves dedicated data processing techniques.

Two such techniques are commonly used to mitigate atmospheric contamination in ground-based CMB experiments. Maximum-likelihood map-making, as implemented by the ACT collaboration (Naess et al. 2025), requires a model of the noise covariance that includes the correlated atmospheric component, which is difficult to construct accurately given the non-stationary nature of the atmospheric contamination, and still poorly constrains some large-scale ambiguous harmonic modes. Filtering methods, such as the filter-bin approach used by the BICEP/Keck collaboration, the SPT collaboration and the QUaD experiment (BICEP2 and Keck Array Collaborations 2016; Dutcher et al. 2021; Pryke et al. 2009), first apply a high-pass filter to remove large-scale noise before projecting the data onto maps. Power spectra computed on the resulting maps are biased by large-scale mode damping or mode-loss. In both cases, recovering information on the largest angular scales remains dif-

⋆ Corresponding author: JulienTang@lbl.gov

ficult. Residual large-scale atmospheric contamination remains typically well-above instrumental white noise.

The two map-making techniques mentioned above operate on a single frequency band at a time. However, atmospheric emission has a characteristic frequency dependence that differs from those of the CMB and astrophysical foreground emissions such as Galactic dust. In this work, we propose an atmosphere template-cleaning approach that exploits this property in a multi-frequency setup, using information from the different bands together with dedicated atmosphere monitors to characterize and subtract the atmospheric signal in the time domain. We address the problem in intensity and demonstrate the efficacy of the method on time-domain simulations. For polarization, we note that reducing the contamination of CMB data streams from unpolarized atmospheric contamination will also reduce the level of intensity-to polarization leakage due to instrumental non-ideality. Quantifying the impact of such cleaning on polarization measurements requires a model of such instrumental imperfections, and is left for future work.

In section 2, we discuss the parameters of the simulation and the atmosphere emission model. In section 3, we present the time-domain atmosphere mitigation pipeline and results on simulated time streams. In section 4, we show the projection of the cleaned time-ordered data (TOD) in map domain and compare the efficacy of the template subtraction with the filter-bin method. We conclude and identify prospects and future work in section 5.

2. Ground-based CMB observation and simulation

Ground-based CMB telescopes are located in some of the driest geographical locations, such as the Atacama plateau in Chile or the South Pole station in Antarctica, where the low precipitable water vapor (PWV) limits atmospheric contamination. The atmosphere both absorbs and emits radiation, primarily through water vapor and molecular oxygen, and this emission adds to the photon flux received by the detectors, increasing the white photon noise. In addition, turbulence, driven by convection and wind shear in the troposphere, generates water vapor inhomogeneities which, owing to the strong water vapor emissivity at microwave frequencies, produces spatially correlated fluctuations in the received power. The local three-dimensional statistics of these fluctuations follow a Kolmogorov spectrum, giving rise to low-frequency noise in the data streams when these structures are swept across the field of view by the telescope scanning and by the wind (Church 1995; Morris et al. 2022; Errard et al. 2015). The atmospheric transmission and emission depend on the observing conditions, in particular the total PWV, and also vary with frequency. The emission lines of water vapor and oxygen punctuate the transmission and define natural atmospheric windows for CMB observations from the ground, as illustrated in Fig. 1. CMB detectors are designed with frequency bands matched to these atmospheric windows.

In addition to atmospheric emission and CMB anisotropies, microwave detector data streams also include fluctuations due to astrophysical foreground emission from Galactic and extragalactic sources, whose amplitude also depends on frequency. Unlike the atmospheric contaminants, these emission components are sky-stationary. Modern focal planes rely on multichroic pixels, dichroic or trichroic, and in particular CMB channels sensitive in two or three of the main atmospheric windows around 90, 150 and 220 GHz (potentially complemented with lower and higher frequency channels for mapping foreground emissions). Several combinations are used in ground-based experiments, such as 90/150 GHz and 220/280 GHz as in the Simons Observatory (Ade et al. 2019) or trichroic 90/150/220 GHz as in SPT-3G (Sobrin et al. 2022) or 30/40 GHz and 220/270 GHz as in the BICEP Array (Hui et al. 2018). The measured time-ordered data (TOD) are then a combination of atmospheric emission, the mm-wave sky (CMB and astrophysical foreground emission), and instrumental noise.

Given the strong correlation of water vapor atmospheric signals across frequency bands, their contribution to the data streams can be treated as those of an additional foreground, with the difference that their fluctuations are a function of time rather than of sky direction.

2.1. Simulated instrumental setup

In this section, we introduce a new instrumental setup designed to observe at multiple frequencies and reconstruct atmospheric fluctuations. This instrumental setup consists of a synthetic hexagonal focal plane with 37 pixels with a narrow field of view of 1°. Actual instruments such as the Simons Observatory Large Aperture Telescope (Abitbol et al. 2025) will deploy $\sim 60,000$ detectors in the 150/220GHZ bands for a 7.8° field of view in CMB bands. Our setup is therefore a simplified toy model for computational simplicity but we can, in principle, scale it up for more realism in a future work. All pixels in our simulation have broad bands centered on 150 GHz and 227 GHz, but other frequency bands could be considered in a similar way.

In addition to these classical dual-frequency pixels, we assume that atmosphere-monitoring pixels, located at the edges of the focal plane and at the boresight, also observe in two additional frequency channels centered at 179 and 188 GHz, probing the wings of the 183 GHz water vapor line. (see Fig. 1). These pixels will enable instantaneous co-pointing observations of both the fixed microwave sky and the fluctuating atmospheric emission. We computed detector sensitivities, for both the dichroic pixels and the atmospheric monitors, using `jbolo`[1], a package derived from `bolocalc` (Hill et al. 2018). We tabulated the sensitivities in Table 1. We note that the choice of these two extra channels in the wings of the water vapor line is for demonstration purposes only, but is logical for monitoring the atmospheric water vapor. However, other choices of multi-frequency focal planes could also be envisaged. The width of the water-vapor monitoring bands considered here is chosen so that the total astrophysical and atmospherical loading in the four bands is approximately the same in the four bands for 1 mm total precipitable water vapor and for observations at 55° elevation. As the present paper is a proof of concept rather than an instrument design, we do not further discuss the exact band choice or exact shapes (we assume top-hat bands for this study), leaving that for future work.

In total, in this model focal plane, there are 30 dichroic detectors for the usual CMB science, and 7 tetrachroic detectors used for separation of the atmosphere. All detectors scan the sky at the same sampling frequency f_s.

2.2. Multi-component microwave sky model

For the proof of concept study presented in this work, we assume a simplified sky model consisting of only two dominant components, the thermal dust and the CMB, in the frequency range of 130-260 GHz. We use the `d9` dust model and `c1` lensed CMB model from the Python Sky Model

[1] `https://github.com/JohnRuhl/jbolo`

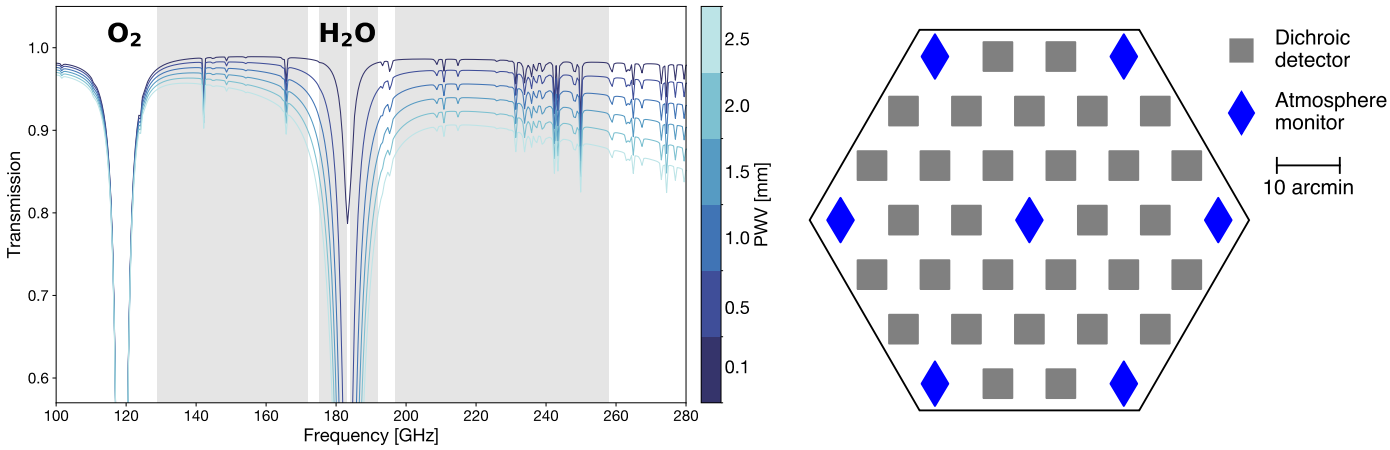

Fig. 1: **Left:** Atmosphere absorption as a function of frequency for weather conditions similar to Atacama and different values of PWV, computed with AtmoCube (Ghosh et al. 2026). The passbands of the detectors are overplotted in gray. **Right:** Layout of the hexagonal multichroic focalplane. The atmosphere-monitoring detectors are indicated in blue.

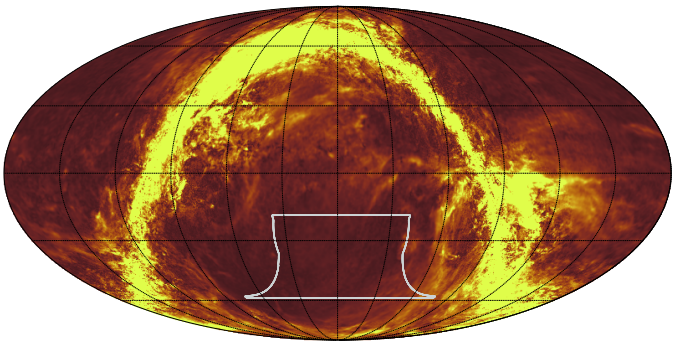

Fig. 2: Observed patch for 10 hours in September from Atacama. We show the target patch on top of the Planck Collaboration et al. (2016) GNILC dust polarized intensity map at 353 GHz.

Table 1: Band centers, bandwidths, and noise-equivalent temperatures (NET) for each frequency band. These values are calculated from the Atacama plateau, for 990 microns of PWV, and at an elevation of 55°.

Band name	Band center [GHz]	Bandwidth [GHz]	NET [$\mu K_{CMB}\ s^{1/2}$]
150GHz	150.5	43.0	201.2
179GHz	179.0	8.0	4354.3
188GHz	188.0	8.0	4143.2
227GHz	227.5	61.0	495.1

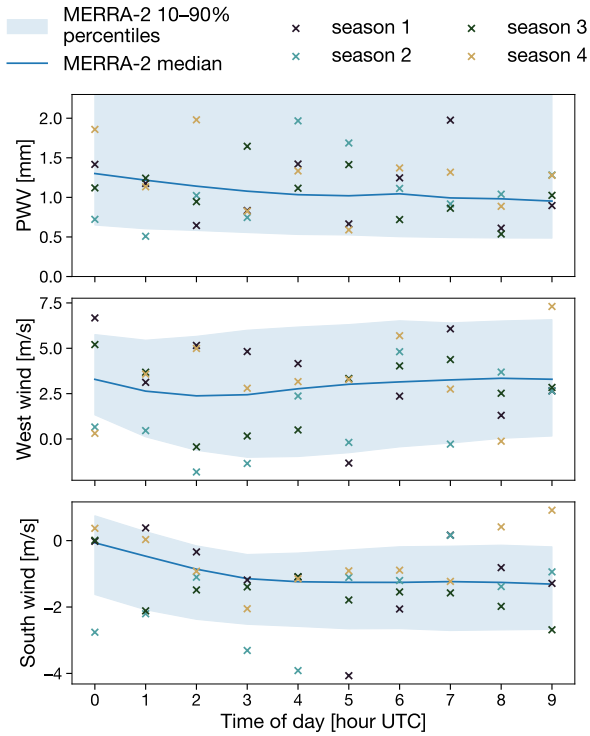

Fig. 3: PWV and wind speed on September 12 for a 10 hour observation. For simplicity, we have simulated 4 realizations of the same observation day. The weather parameters are drawn from a distribution calibrated on MERRA-2 data. We have selected realizations with PWV under 2 millimeters.

(The Pan-Experiment Galactic Science Group et al. 2025). The `d9` dust model uses the Planck Collaboration et al. (2020) GNILC dust map at 353 GHz as a dust amplitude template. This template is then rescaled to other frequencies assuming a modified blackbody frequency scaling with a spectral index of 1.48 and a blackbody temperature of 19.6 K. The `c1` lensed CMB map is produced with cosmological parameters from Planck Collaboration et al. (2016).

Although somewhat oversimplified, the two component sky model with fixed dust scaling captures the first-order properties of the microwave sky in the frequency range of interest for our study. Small corrections due to variations of the dust emission law as a function of sky direction, as well as contributions from other subdominant sky components, are ignored for the moment. The quantification of their impact is left to future work, but we note that timelines can be corrected for astrophysical foreground components in an iteration of the pipeline, by "re-observing" foreground maps obtained after a first iteration of the entire data pipeline, and subtracting their contribution from the data streams for an iteration of the map-making pipeline. One could also ob-

serve with more frequency bands to deal with increased sky and atmosphere complexity.

2.3. Atmosphere simulation

The atmospheric contribution is modeled by generating a static, three-dimensional realization of the water-vapor fluctuation field above the telescope and sampling it along each detector's line of sight. Following Church (1995), the field is treated as a Gaussian random field whose spatial correlations combine two physically motivated ingredients: an exponential decrease of the fluctuation amplitude with altitude, which concentrates the emission near the ground, and a Kolmogorov turbulence spectrum that sets the structure across scales. Under the frozen-flow approximation, the field is static and the whole volume is simply displaced across the line of sight by a constant wind. This is done in practice using the atmosphere simulation module that is part of the Time-Ordered Astrophysical Scalable Tools (`TOAST`[2]) package.

`TOAST` builds the field in direct space: it constructs the covariance matrix between the grid cells crossed by the beam and draws a correlated realization from it. Correlations between detectors, which probe largely the same volume of atmosphere, arise naturally.

An originally dimensionless fluctuation field is converted into a detector signal through a per-detector scaling that depends on observing frequency and precipitable water vapor (PWV). In the optically-thin regime, the emission is linearized about a fixed mean water-vapor column, so this scaling reduces to the atmospheric absorption convolved with the detector bandpass and depends only on the frequency band. The absorption is obtained from the atmospheric transmission at the microwaves (ATM) model (Pardo et al. 2001). Weather parameters such as the PWV, wind speed, and wind direction are drawn from distributions derived from MERRA-2 reanalysis data (Gelaro et al. 2017), binned by month and hour of day, and the resulting simulations are calibrated against the ACT data. Implementation details can be found in the `TOAST` documentation.

2.4. Observing schedule and weather conditions

We simulate observation of the sky as visible on September 12, from midnight to 10:00 UTC, for a telescope located on the Atacama plateau. The schedule consists of ten one-hour constant-elevation scans at an elevation of 55°, each spanning 90° in azimuth, with the first five targeting the rising field and the last five the setting field. During each hour, the telescope performs back-and-forth scans, alternating between two scanning directions (left-to-right and right-to-left), with flagged turnarounds in between. We adopt a scanning speed of 1°/s and a sampling frequency of 40 Hz. The resulting sky footprint is shown in Fig. 2.

We simulate four realizations of this same day under different weather conditions, all with a PWV below 2 mm (Fig. 3), which could correspond to either four observations during different seasons, or observations in contiguous days obtained at the same sidereal time (rather than local time). For each hour of the schedule, the PWV, wind speed, and wind direction are drawn from the corresponding September, hourly MERRA-2-calibrated distributions. This lets us focus the map-based analysis on a single patch while still averaging down the atmospheric residuals, which are uncorrelated between observing sessions.

[2] `https://github.com/hpc4cmb/toast`

2.5. Simulated timelines

We generate the synthetic observations with `TOAST`. For each of the four observing sessions, the different contributions to the TOD are created separately: the sky-synchronous signal, the instrumental white noise, and the atmospheric fluctuations.

The sky-synchronous signal is obtained by scanning the foreground and CMB maps of subsection 2.2, taking into account the correspondence between local azimuth and elevation and fixed-sky coordinates as a function of the Earth's rotation. The sensitivity of each detector is given by a noise equivalent temperature (NET) in units of μK s$^{-1/2}$ (see table 1). The instrumental white noise timeline at frequency ν, sampled with a sampling period t_s, is generated independently for each detector as a Gaussian realization. The sample variance σ_ν^2 is obtained from the NET as $\sigma_\nu^2 = \mathrm{NET}(\nu)^2/t_s$. For a given sky pixel observed simultaneously in N_{bands} frequency bands, we define the corresponding noise covariance matrix $\mathbf{N}$ in frequency space, with entries $\mathrm{N}_{\nu\nu'} = \sigma_\nu^2\,\delta_{\nu\nu'}$, which is diagonal and has shape $(N_{\mathrm{bands}}, N_{\mathrm{bands}})$. The atmospheric fluctuations are correlated between detectors and generated from the emission model of subsection 2.3.

We then coadd these contributions to form the simulated detector TOD. Each of them can also be passed individually through the same linear pipeline, which allows us to isolate and quantify the pipeline's effect.

3. Atmosphere mitigation at the time stream level

We now turn to the description of the time-domain processing pipeline implemented for estimating the astrophysical signal starting from the TOD, exploiting the frequency dependence and the time-correlation of the atmospheric emission to reduce its contamination of the maps of astrophysical emission of interest. For the rest of the analysis, we concentrate on the unpolarized, intensity-only data streams.

3.1. Data model

The TOD correspond to the variation of intensity measured by the focal plane bolometers as they scan the sky. The measured signal for a given frequency band includes a combination of atmosphere emission, astrophysical sky-signal, and noise. The vector of TOD samples can be written as

$$d_{\nu t} = \sum_p \sum_c P_{tp} F_{\nu c} m_{cp} + x_{\nu t} + n_{\nu t}, \tag{1}$$

where $d_{\nu t}$, $x_{\nu t}$ and $n_{\nu t}$ are the total TOD, the atmospheric signal, and the noise at frequency ν and at time t respectively, m_{cp} is a map of component c in pixel p, P_{tp} is a pointing matrix identifying which pixel p is visited at time t as a function of the focal plane geometry and the scan strategy, and $F_{\nu c}$ is a mixing matrix for the sky components indexed by c, assumed to be constant over the region of the sky that is mapped during the observations.

In all generality, we could also consider the atmospheric emission to be the sum of several components j (e.g. water vapor and temperature fluctuations, clouds), so that $x_{\nu t} = \sum_j G_{\nu j} s_{jt}$. Writing $\sum_p P_{tp} m_{cp} = s_{ct}$ we can treat the sky components and atmosphere components on an equal footing, and write

$$\boldsymbol{d}_t = \mathbf{A}\boldsymbol{s}_t + \boldsymbol{n}_t, \tag{2}$$

where $\boldsymbol{d}_t$ is the collection of data samples at time t for all frequency bands, $\boldsymbol{s}_t$ the collection of time samples at time t for all

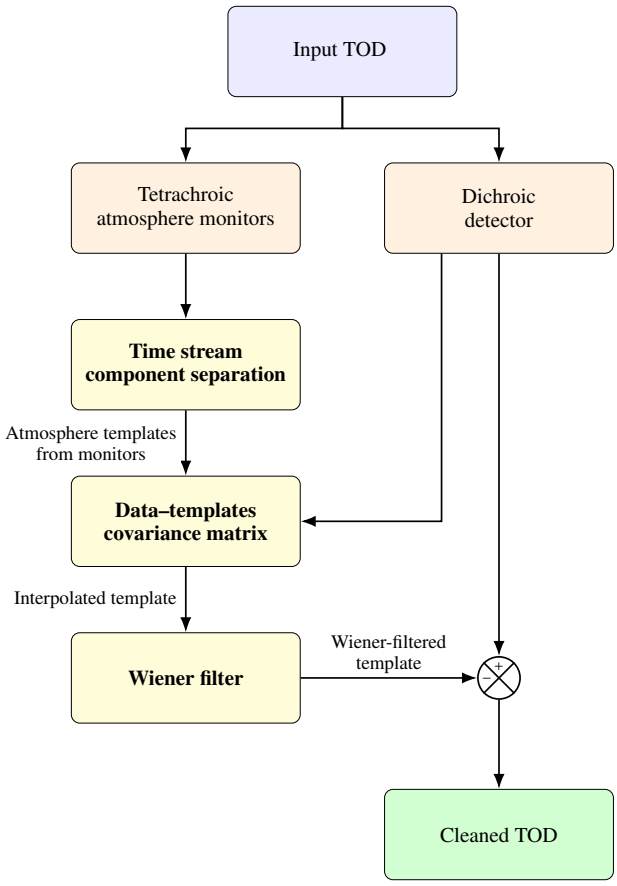

Fig. 4: Atmosphere mitigation pipeline at the time stream level.

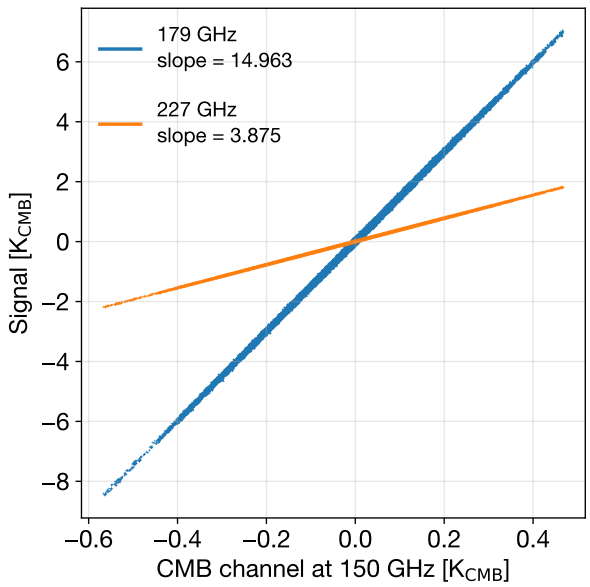

Fig. 5: Detector signal versus the 150 GHz CMB channel for the 179 and 227GHz frequency bands, using the full time streams including instrumental noise and astrophysical signal. The 188GHz channel is closely superimposed with the 179GHz, with almost identical slopes (14.963 for the 179GHz and 14.958 for the 188GHz).

components (here $N_{\rm comp} = 3$, CMB, dust and one single component of atmosphere), and $\boldsymbol{n}_t$ noise samples in all frequency bands. The mixing matrix $\mathbf{A} = [\mathbf{F}|\mathbf{G}]$ now is a fixed, $N_{\rm bands} \times N_{\rm comp}$ matrix that is assumed to be time-independent.

3.2. Atmosphere mitigation

The mitigation strategy proceeds in three steps, summarized in Fig. 4:

1. For each atmosphere-monitoring pixel of the focal plane, we perform a TOD component separation and create a template for the atmospheric emission as a function of time.
2. For each standard detector, we fit the atmospheric contamination with a linear combination of the previously obtained atmospheric TOD templates, using their correlation with the data stream for the detector being considered.
3. The atmosphere template obtained for the detector is Wiener-filtered to reduce the contamination by residual white noise from atmosphere-monitoring pixels before subtraction from the detector original TOD.

We discuss these steps in more detail below.

3.2.1. Component separation

In a first step, we consider the four data streams for each of the seven tetrachroic pixels and look for the solution of Eq. 2.

We begin with the calibration (estimation) of the mixing matrix $\mathbf{A}$. We make the approximation that it is constant over one-hour-long observations. We also assume here that the sky mixing matrix $\mathbf{F}$ is known. This leaves only the part $\mathbf{G}$ of the mixing matrix that corresponds to the atmosphere to be estimated (a single vector for one-dimensional atmosphere as assumed here). As atmospheric emission is the dominant contribution by orders of magnitude, we simply use the slope between TODs at different frequencies.

With this estimate of the mixing matrix and the cross-frequency noise covariance, the generalized least-squares solution for the atmosphere monitor pixels is given by:

$$\hat{\boldsymbol{s}} = \left(\mathbf{A}^T\mathbf{N}^{-1}\mathbf{A}\right)^{-1}\mathbf{A}^T\mathbf{N}^{-1}\,\boldsymbol{d} \tag{3}$$

where $\hat{\boldsymbol{s}}^T = \left(\hat{s}^{\rm CMB} \quad \hat{s}^{\rm dust} \quad \hat{s}^{\rm atm}\right)$ are the component templates and the third entry is the atmospheric template $\hat{s}^{\rm atm}$ for a monitoring pixel. An important property of the component separation step is that the template consists of atmosphere and projected white noise, with negligible residual astrophysical sky signal.

3.2.2. Interpolation and Wiener filtering

The component separation stage in 3.2.1 produces 7 templates $\hat{\boldsymbol{s}}_1^{\rm atm}, \ldots, \hat{\boldsymbol{s}}_7^{\rm atm}$ which sample the atmospheric signal across the focal plane. Given the relatively small field of view considered here, the atmospheric fluctuations seen by neighboring detectors are strongly correlated.

The correlations depend on the scanning direction, since they change with the wind speed relative to the telescope. The relative wind results both in a change in the spatial correlations between a given pixel and its neighbors, and in a shift of the power spectrum toward higher frequencies as the relative wind speed increases. Therefore, we treat separately left-to-right going scans and right-to-left going scans.

Consider a scanning direction. We set to zero the data streams outside of the corresponding scanning intervals. The

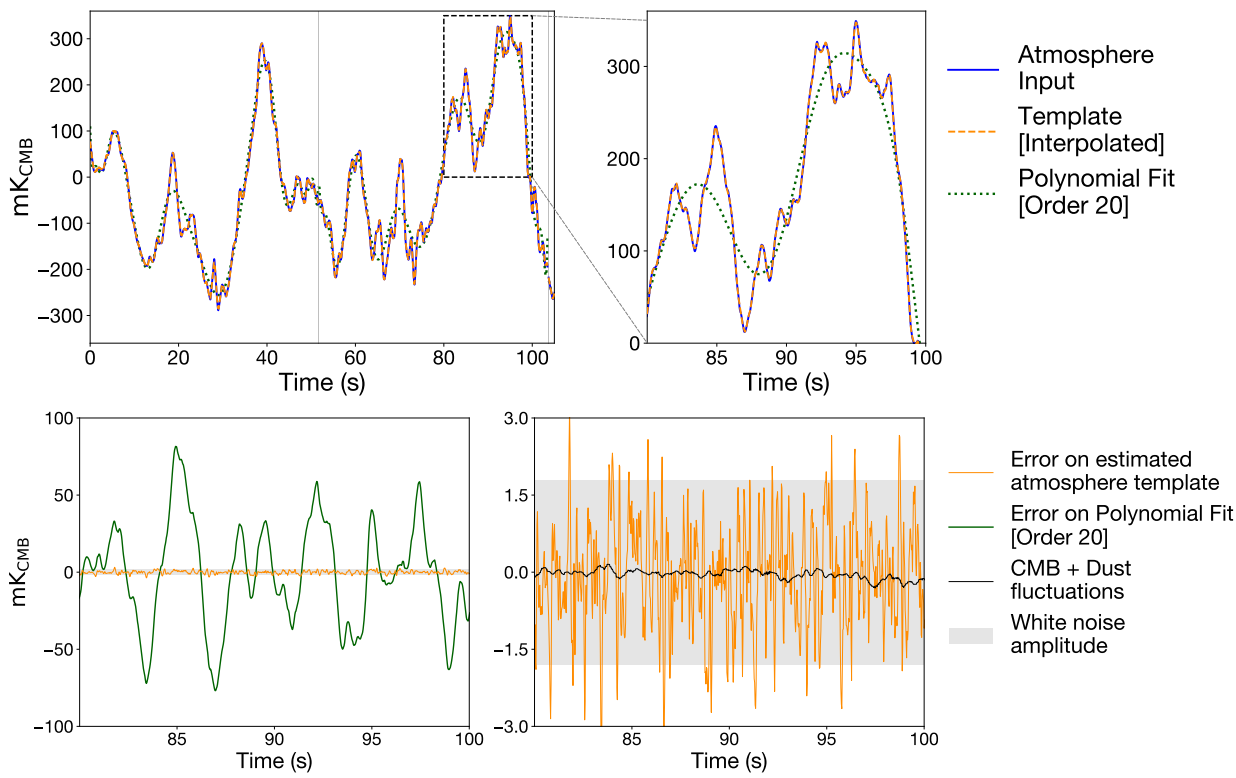

Fig. 6: Comparison of template interpolation and filtering. **Top:** the templates compared to the input signal; in each scan, a polynomial of order 20 is fitted and removed from the data. For sharp fluctuations of the atmosphere, we clearly see that the polynomial does not fit the atmosphere input well, contrarily to the template. For intensity, the difference between the input signal and the polynomial fit is large. **Bottom:** the errors on the templates, compared to CMB and dust fluctuations and the white noise level.

stacked vector $\boldsymbol{y}_i^T = \begin{pmatrix} d_i^{\rm det} & \hat{s}_1^{\rm atm} & \cdots & \hat{s}_7^{\rm atm} \end{pmatrix}$ containing the TOD for the i-th detector and the atmospheric templates obtained in the previous steps is a combination of astrophysical signal and noise, where now all the atmosphere templates are dumped in the noise vector:

$$\boldsymbol{y}_i = \boldsymbol{M}\, s_i^{\rm sky} + \boldsymbol{n}_i', \tag{4}$$

where $\boldsymbol{M}^T = \begin{pmatrix} 1 & 0 & \cdots & 0 \end{pmatrix}$ encodes that only the first entry of $\boldsymbol{y}_i$ (i.e. the bolometer data) contains the astrophysical signal, and the vector $\boldsymbol{n}_i'^T = \begin{pmatrix} n_i^{\rm w} + s_i^{\rm atm} & \hat{s}_1^{\rm atm} & \cdots & \hat{s}_7^{\rm atm} \end{pmatrix}$ models the total "noise" (anything non-astrophysical), including atmosphere emission in the detector of interest and all the atmosphere templates obtained with the atmospheric monitors.

Since the atmosphere is much brighter than the sky signal, it allows us to directly estimate the noise covariance matrix of 4:

$$\mathbf{C}_i = \langle \boldsymbol{n}_i' \boldsymbol{n}_i'^T \rangle \approx \langle \boldsymbol{y}_i \boldsymbol{y}_i^T \rangle \tag{5}$$

where the brackets indicate averaging over time samples.

The weights that minimize the variance of $\hat{s}_i^{\rm sky}$ in Eq. (4) read

$$\boldsymbol{w}_i^T = [\boldsymbol{M}^T \mathbf{C}_i^{-1} \boldsymbol{M}]^{-1} \boldsymbol{M}^T \mathbf{C}_i^{-1}. \tag{6}$$

and to retrieve the interpolated template, we apply these weights to the concatenated templates:

$$\hat{s}_i^{\rm atm} = \boldsymbol{w}_i^T \begin{pmatrix} 0 & \hat{s}_1^{\rm atm} & \cdots & \hat{s}_7^{\rm atm} \end{pmatrix}^T. \tag{7}$$

Since the monitor templates in Eq. (7) contain residual white noise after the component separation, the interpolated template $\hat{s}_i^{\rm atm}$ is also contaminated by white noise. In order to avoid injecting this white noise component when subtracting the template from the data, we Wiener filter the templates before subtraction.

The atmosphere fluctuations dominate template signals on large scales, while residual white noise from the atmosphere monitors dominate on the smaller scales. We estimate the power spectral density averaged on scans depending on their direction and identify a white noise plateau at high frequencies. Denoting by $\mathcal{P}_i(f)$ the PSD of the template $\hat{s}_i^{\rm atm}$ and by $\mathcal{N}_i^{\rm w}$ the white-noise level estimated from its high-frequency plateau, the Wiener filter reads

$$\mathcal{W}_i(f) = 1 - \frac{\mathcal{N}_i^{\rm w}}{\mathcal{P}_i(f)} = \frac{\mathcal{S}_i(f)}{\mathcal{S}_i(f) + \mathcal{N}_i^{\rm w}} \tag{8}$$

with $\mathcal{S}_i(f) \equiv \mathcal{P}_i(f) - \mathcal{N}_i^{\rm w}$. This is optimal under the assumption that signal and noise are uncorrelated and, assuming perfect correlation between the atmospheric templates and the atmospheric contamination in detector i, returns the minimum-mean-square-error estimate of the atmospheric component. The atmosphere-cleaned TOD in a science band is finally obtained as

$$\hat{d}_i = d_i - \mathcal{F}^{-1}\Big[\mathcal{W}_i(f)\, \tilde{s}_i^{\rm atm}(f)\Big] \tag{9}$$

where $\tilde{s}_i^{\rm atm}$ is the Fourier transform of $\hat{s}_i^{\rm atm}$ and $\mathcal{F}^{-1}$ the inverse Fourier transform. Finally, the output cleaned TOD is the sum of the cleaned TOD for each scanning direction.

3.3. Comparison with the Filter-Bin approach

Fig. 6 compares, at the time stream level, different estimates of the atmospheric signal, and Fig. 7 compares residual power

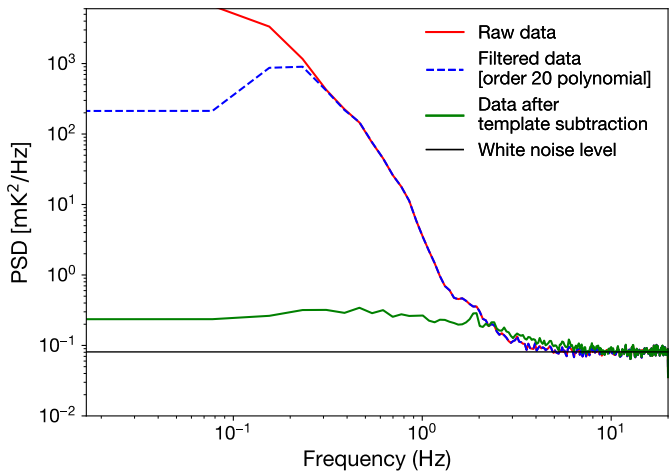

Fig. 7: Power Spectral Density of a time stream for a detector in the 150GHz band: before processing, after polynomial filtering and after template subtraction.

spectra in time domain. We compare our new method described above with the polynomial-fitting technique commonly used in filter-bin map-making. For the later method, we fit order-20 polynomials over scan intervals of about 50 seconds to estimate the large scale atmospheric fluctuations. This is similar to the pipeline used in SPT (Dutcher et al. 2021) where a 19-th order Legendre polynomial is fitted for each scan of 100 seconds.

Contrarily to template subtraction, the subtraction of a polynomial fit also removes some of the astrophysical signal. This will result in a transfer function which is discussed in Sec. 4. The polynomial fit recovers some of the general trend but, for data timelines that include intensity, it fails on scales of a few seconds, where the atmosphere can vary sharply.

In figure 6, we also show the difference between the input atmosphere-only time stream and each template, as a measure of the residual atmosphere. For the polynomial fit, the error on the estimated atmosphere is of the order of a fraction of the atmospheric fluctuations themselves, whereas for the template interpolation the residuals have an amplitude closer to the white-noise level. For polarization measurements using pair differencing, polynomial fit residuals can be reduced by an order of magnitude or two, close to the instrumental noise level, but still at the price of some filtering of the astrophysical of interest. In contrast, the template interpolation described earlier recovers most of the fluctuations, whether the signal of interest is intensity or polarization.

The improvement is also visible in the detector PSD before and after correction as illustrated in Fig. 7, using either template subtraction or polynomial filtering. Polynomial filtering yields a moderate improvement on large scales, but intermediate scales (smaller than a few seconds) remain entirely contaminated by the atmosphere. For the time stream cleaned with the interpolated template, the power decreases by four orders of magnitude, along with a reduction of the slope on the Kolmogorov spectrum. We note, however, a slight excess around 5Hz in the residuals obtained with our method. This is due to the assumption that the templates are perfectly correlated with the atmospheric contamination in each detector. In reality, a slight decorrelation is induced by the different lines of sight of distinct focal plane pixels through the atmosphere. As a future improvement, one could estimate this decorrelation and further filter the atmosphere templates for an optimized correction. We leave this refinement for future work.

4. Map results and comparison of methods

In this section, we quantify the efficacy of the time-domain cleaning pipelines at map and power spectrum level. We will compare the atmosphere template correction with the polynomial filter by propagating the TODs to maps and power spectra. As a control, we also propagate the TODs without any cleaning to map and spectrum. In all cases, the TODs are projected into maps following the procedure described in subsection 4.1, at $N_{\rm side} = 1024$.

4.1. Inverse Variance Binning

The same map-making procedure is applied to all TOD processing pipelines. We assume a white-noise model for the TOD, with no spatial or temporal correlations, and combine the individual observations with an inverse-variance weighting.

The survey consists of $N_r = 4$ observing days sharing an identical schedule and overlapping footprints, each covering the same ten hourly patches. For a given hour h, the pointing matrix $\mathbf{P}_h$ is therefore common to all seasons and the hourly survey footprint is described by $\Omega_h(p) \in \{0, 1\}$, which is equal to 1 for pixels observed in hour h. Denoting $\mathbf{d}_h^r$ the TOD for hour h and season r, we bin all detector samples into a map i.e. averaging the samples in each pixel:

$$m_h^r = \left(\mathbf{P}_h^T \mathbf{P}_h\right)^{-1} \mathbf{P}_h^T \mathbf{d}_h^r. \tag{10}$$

The ten combined hourly footprints partially overlap on the sky to generate the coverage map outlined in Fig. 2.

As the weather changes from one hour to the next, the atmospheric noise level varies between hourly maps, predominantly on large scales. First, as the atmosphere is uncorrelated between days, we average each hourly map over the N_r days to get an average map $\bar{m}_h$ (lowering the noise variance by a factor N_r). Second, we estimate the residual noise level of each averaged map by applying a low-pass filter that retains $\ell \leq 300$, isolating the large angular scales where the atmospheric noise dominates, and take the standard deviation of the filtered map over the footprint,

$$\sigma_h = \sigma\left(\bar{m}_h^{\rm filtered}\big|_{\Omega_h}\right). \tag{11}$$

Finally, we coadd the ten hourly maps with an inverse-variance weighting. Defining the hourly weight map $w_h = \Omega_h/\sigma_h^2$ and the coadded map is

$$\hat{m} = \frac{\sum_h w_h \bar{m}_h}{\sum_h w_h}. \tag{12}$$

We produce maps of the unprocessed, template-cleaned, and poly-filtered TODs with this common binning pipeline. In the following, we refer to these maps as simple-bin, template-cleaned and filter-bin maps respectively.

4.2. Maps and spectra

In Fig. 8, we compare the reconstructed maps after template subtraction, with different integration time and the input sky signal (CMB and dust) map. The sky emission features are clearly visible in each of the maps and the contamination by noise and residual atmosphere decreases with integration time. For comparison,

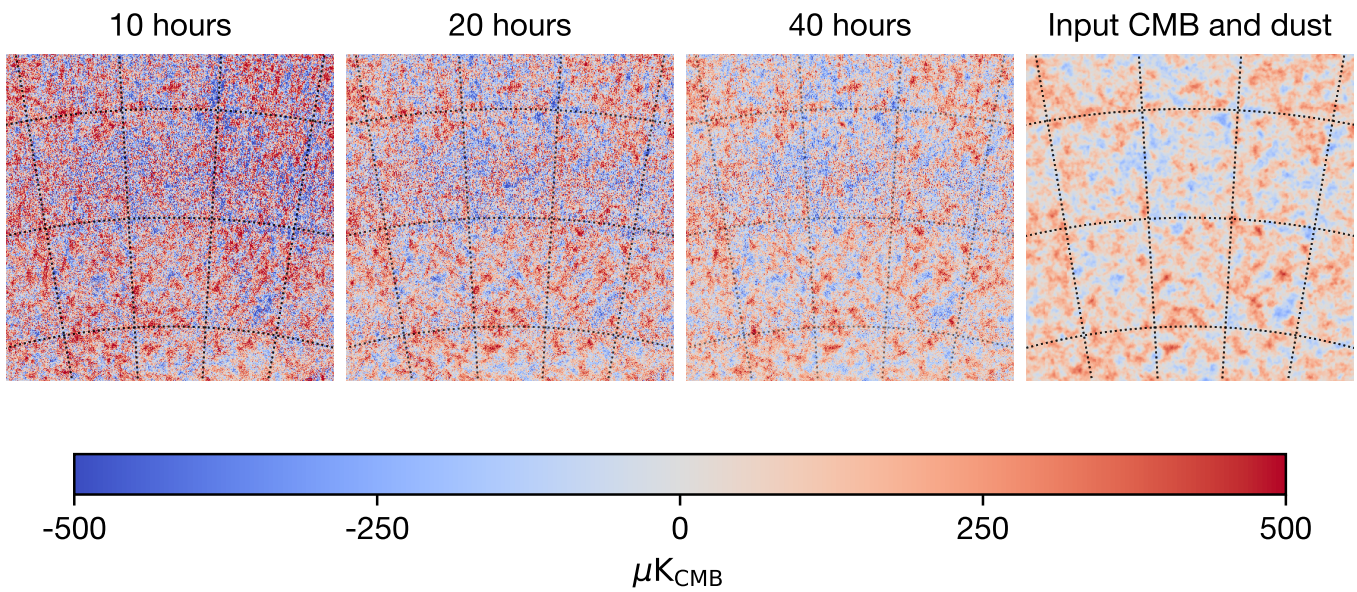

Fig. 8: Reconstructed maps after atmosphere template subtraction and inverse-variance binning. **First to third panels:** reconstructions with 10, 20, and 40 hours of integration time, respectively. **Rightmost:** input CMB and dust map. All maps share the same color scale.

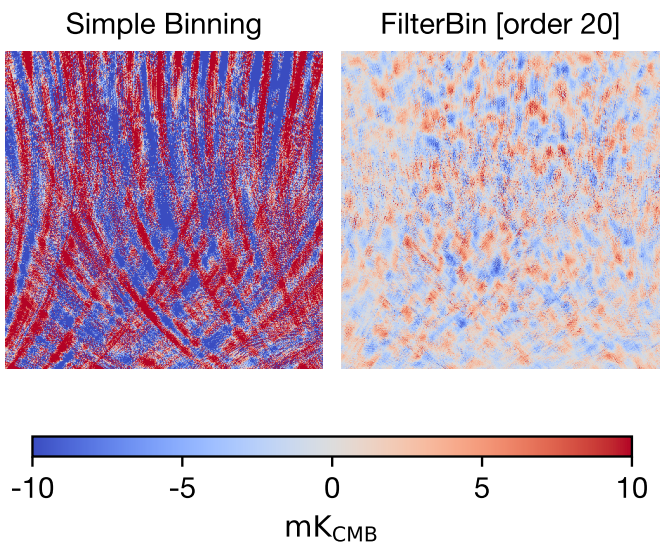

Fig. 9: Output maps for 40 hours of observation after simple binning or with filter-bin. Note the color scale now in mK.

the same maps after simple-bin and filter-bin are shown in Fig. 9. These maps are completely dominated by atmosphere residuals and the original signal is not discernible at all. Notice in the simple-bin map how the atmosphere is projected along the scanning directions as can be seen with the vertical stripes. Large-scale modes along the direction of scans can result in smaller-scale modes in the orthogonal direction, leading to leakage of power from large to small scales.

In the case of filter-bin, the filter suppresses some of the sky signal along with the atmosphere. This suppression is quantified by a transfer function, which we define in the power-spectrum domain as $T_\ell = C_\ell^{\rm out}/C_\ell^{\rm in}$, the ratio of the output to input signal power spectra. The template-subtracted and raw maps have $T_\ell = 1$ by construction, whereas the filter-bin maps have $T_\ell \leq 1$ and must be corrected by T_ℓ before comparison.

In Fig. 10 we show the angular power spectra of the residual maps, $C_\ell^{\rm res}$, obtained as the difference between each output map and the input sky signal. Consistently with Fig. 8, we see that the residuals for the template-cleaned map are comparable to the input sky signal or lower, with a signal-to-noise ratio above one up to $\ell \sim 300$, and average down with integration time as the atmosphere is uncorrelated between days. In contrast, the simple-bin and filter-bin residuals remain orders of magnitude above the sky signal at all scales. For filter-bin, the residual plotted in the spectral domain is corrected for the transfer function T_ℓ, evaluated on signal-only simulations, which decays below $\ell \sim 200$; even so, the residual stays up to four orders of magnitude above the target signal.

We note that for all three methods, residual atmosphere contamination increases not only the noise on large scales in the maps, but also at high-ℓs. As already mentioned above for the filter-bin method, this is due to projection effects which generate small-scale fluctuations across the scanning directions from large scale fluctuations along the scans. We also note in Fig. 10 that both the simple-bin and the filter-bin spectra share a characteristic dip followed by a bump at intermediate scales. This feature arises from the sparsity of the focal plane combined with the survey strategy. At the map resolution used here, the angular separation between detectors exceeds the pixel size, so for constant-elevation scans the footprint of a single scan consists of parallel lines separated by unvisited pixels. As the detector time streams are correlated through the atmospheric emission, an excess of power appears at the characteristic scale set by the inter-detector separation. Superimposed on the atmospheric spectrum, which decays with multipole, this produces the observed dip-and-bump feature.

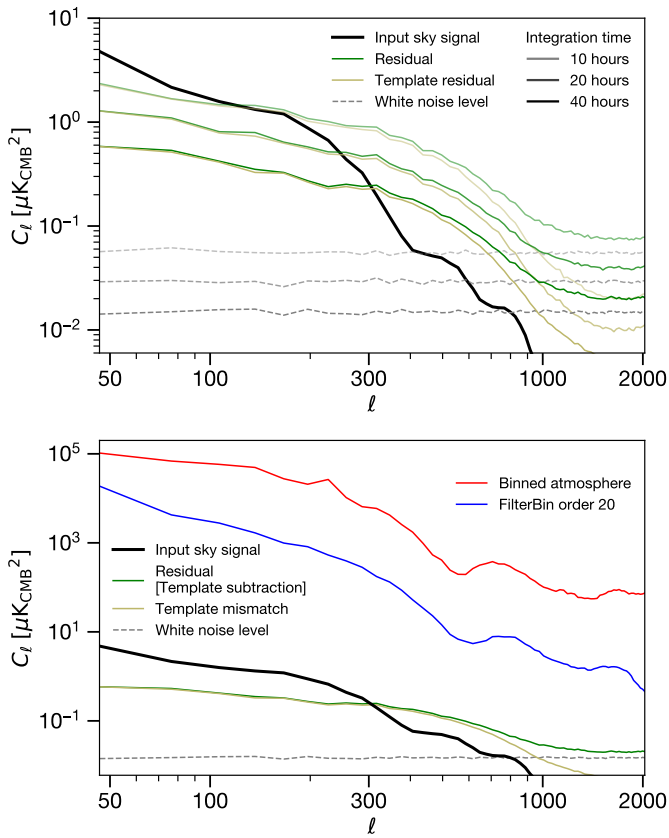

Fig. 10: Angular power spectra of the residual maps (output − input sky signal). **Top:** template-subtraction residuals for 10, 20, and 40 hours of integration, compared with the input sky signal and projected white noise. **Bottom:** residuals for simple binning and filter-bin. Note the difference in y-axis range between the two panels.

4.3. Atmospheric decontamination factor

To quantify the quality of atmosphere removal directly, we define an atmospheric decontamination factor, in analogy to a "delensing factor" for lensing correction in CMB B-mode maps) as

$$A_\ell^{\rm atm} := \frac{C_\ell^{\rm res}/T_\ell - N_\ell}{C_\ell^{\rm atm}}, \tag{13}$$

where $C_\ell^{\rm res}$ is the residual-map spectrum, N_ℓ the projected white-noise spectrum, $C_\ell^{\rm atm}$ the binned atmosphere spectrum, and T_ℓ the transfer function (equal to unity for all pipelines considered here except filter-bin). In the limit where the pipeline reconstructs perfectly the atmosphere signal, the power spectra of the residual maps is only projected white noise, and $A_\ell^{\rm atm} = 0$. This atmospheric decontamination factor measures the residual fraction of the atmosphere emission in the output map. As shown in Fig. 11, template subtraction suppresses the atmosphere to the 10^{-5} level across $30 \leq \ell \leq 300$. Averaged over this range, $A^{\rm atm} = \langle A_\ell^{\rm atm}\rangle_{[30,300]}$ is 1.3×10^{-5} for template subtraction against 5.6×10^{-2} for filter-bin, a factor of ~ 4000 improvement.

5. Conclusion and future work

In this work, we have introduced a multi-frequency, time-stream-level approach to mitigate atmospheric contamination in ground-based CMB observations. By dedicating a subset of detectors to atmosphere monitoring and exploiting the frequency correlations of the atmospheric emission, we built time-domain atmosphere templates, interpolated them across the focal plane, and subtracted them from the science detectors after Wiener filtering. Unlike filtering-based methods, this procedure leaves the astrophysical signal untouched in the TOD and is therefore free of the transfer function that biases filter-bin maps.

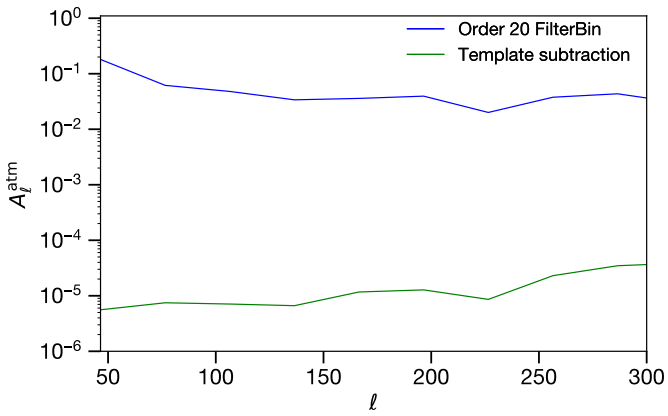

Fig. 11: Atmospheric decontamination factor $A_\ell^{\rm atm}$ (Eq. 13), comparing template subtraction and filter-bin over $30 \leq \ell \leq 300$. Lower values indicate more effective atmosphere removal.

On simulated observations reproducing Atacama-like conditions, the method recovers the CMB and dust signal with 30 science detectors in less than two days of total observation. We quantify its performance through an atmospheric decontamination factor $A_\ell^{\rm atm}$, and find an average value of 1.3×10^{-5} over the range $\ell \in [30, 300]$, compared to 5.6×10^{-2} for a filter-bin pipeline, an improvement of more than three orders of magnitude on the largest scales. We further find that this residual scales as the inverse of the survey time, as the atmosphere decorrelates between observations.

Several extensions are left for future work. Our proof of concept assumes an atmosphere mixing vector that is constant across frequencies and, in the simulation, exact by construction; a realistic treatment must also account for the true frequency dependence of the atmospheric absorption, in particular near the 183 GHz water line, which departs from a simple rescaling. We have also restricted the analysis to intensity and to a deliberately simplified sky model; extending the method to polarization and to a more complex astrophysical sky are natural next steps. Finally, the correlated residuals left in the cleaned TOD will need to be propagated properly, for instance within a maximum-likelihood map-making framework.

We also note that neither the specific selection of frequency bands used in the present work, nor the fact that all bands share the same focal plane pixel for the atmospheric monitors, are critical for the feasibility of our method. The particular choice considered in this paper just simplifies the practical implementation of a pipeline solution. The method could be extended to other multi-frequency instrumental designs, which could be optimized to separate any specified number of astrophysical and atmospheric components. One could also use external foreground maps to help with the separation of atmospheric contamination from astrophysical foregrounds, or implement an iterative analysis, potentially making an extension of this approach feasible

with dichroic focal plane pixels. We leave to future work investigations along these potential paths.

Acknowledgements. JT, SG and JD thank Aritoki Suzuki for useful comments on the design of a multichroic pixel. Some of the results in this paper have been derived using the healpy and HEALPix packages. This research used resources of the National Energy Research Scientific Computing Center (NERSC), a Department of Energy User Facility (project mp107, 2025-2026).

References

Abitbol, M., Abril-Cabezas, I., Adachi, S., et al. 2025, Journal of Cosmology and Astroparticle Physics, 2025, 034
Ade, P. et al. 2019, Journal of Cosmology and Astroparticle Physics, 2019, 056
BICEP2 and Keck Array Collaborations. 2016, Astrophys. J., 825, 66
Church, S. E. 1995, MNRAS, 272, 551
Dutcher, D., Balkenhol, L., Ade, P. A. R., et al. 2021, Phys. Rev. D, 104, 022003
Errard, J., Ade, P. A. R., Akiba, Y., et al. 2015, The Astrophysical Journal, 809, 63
Gelaro, R. et al. 2017, Journal of Climate, 30, 5419
Ghosh, S., Delabrouille, J., Le Lorec, V., Tang, J., et al. 2026, in preparation
Hill, C. A., Bruno, S. M., Simon, S. M., et al. 2018, in Millimeter, Submillimeter, and Far-Infrared Detectors and Instrumentation for Astronomy IX, ed. J. Zmuidzinas & J.-R. Gao (SPIE), 137
Hui, H., Ade, P. A. R., Ahmed, Z., et al. 2018, in Millimeter, Submillimeter, and Far-Infrared Detectors and Instrumentation for Astronomy IX, ed. J. Zmuidzinas & J.-R. Gao, Vol. 10708, International Society for Optics and Photonics (SPIE), 1070807
Morris, T. W., Bustos, R., Calabrese, E., et al. 2022, Phys. Rev. D, 105, 042004
Naess, S. et al. 2025, Journal of Cosmology and Astroparticle Physics, 2025, 061
Pardo, J., Cernicharo, J., & Serabyn, E. 2001, IEEE Transactions on Antennas and Propagation, 49, 1683
Planck Collaboration, Ade, P. A. R., Aghanim, N., et al. 2016, A&A, 594, A13
Planck Collaboration, Akrami, Y., Ashdown, M., et al. 2020, A&A, 641, A4
Pryke, C., Ade, P., Bock, J., et al. 2009, The Astrophysical Journal, 692, 1247
Simon, S. et al. 2026, in preparation
Sobrin, J. A. et al. 2022, The Astrophysical Journal Supplement Series, 258, 42
The Pan-Experiment Galactic Science Group, Borrill, J., Clark, S. E., et al. 2025, The Astrophysical Journal, 991, 23